1940 *Macromolecules* **2003,** *36,* 1940−1954

In-Situ Studies of Structure Development during Deformation of a Segmented Poly(urethane−urea) Elastomer

Fengji Yeh and Benjamin S. Hsiao*

Department of Chemistry, State University of New York at Stony Brook,
Stony Brook, New York 11794-3400

Bryan B. Sauer

DuPont Central Research & Development, Experimental Station, Wilmington, Delaware 19880-0356

Samuel Michel and Heinz W. Siesler*

Department of Physical Chemistry, University of Essen, D45117 Essen, Germany

Received September 6, 2002; Revised Manuscript Received January 8, 2003

ABSTRACT: The structural development of a segmented poly(urethane−urea) (PUU) elastomer containing a low concentration of hard segment during deformation was studied by simultaneous mechanical and optical measurements (rheooptical techniques). Specifically, in-situ wide-angle X-ray diffraction and small-angle X-ray scattering using synchrotron radiation and time-resolved Fourier transform infrared spectroscopy were applied to investigate the segmental orientation of PUU chains during cyclic elongation and recovery. Formation of two different domain microstructures is characterized with changes in strain. These microstructures consist of lamellar hard domains and highly stressed nanofibrils consisting of alternating hard and crystalline soft domains. By comparing the X-ray scattering and vibrational spectroscopic data, a morphological model of hard- and soft-segment microphase separation, orientation, and strain-induced crystallization in the soft segments was obtained.

Introduction

Polyurethanes (PU) were first discovered by Otto Bayer and co-workers in 1937[1] as a competitive response to the work on nylon by scientists from Du Pont de Nemours. Because of the versatility of polyurethane chemistry, this class of polymer can be produced into an extremely broad spectrum of materials ranging from flexible foams to thermoplastic elastomers.[2−4] In this study, we are interested in a unique class of polyurethane elastomers, poly(urethane−urea) (PUU), which exhibits properties such as high tensile strength, elongation to break, hardness, and modulus in comparison with other types of thermoplastic elastomers. The unique elastic properties are due to the microphase separation of hard and soft segments into domain structures during materials preparation and processing. These domains usually contain polar functionalities from hard segments that can form very strong chemical or physical bonds. As a result, PUU is not thermoplastic and can be processed only from solution, which is quite different from segmented polyurethanes. (They can be processed either from solution or thermally.)

The typical polyurethane elastomer is a linear block copolymer containing three main components: a polyol, a diisocyanate, and a chain extender. Depending on the nature and the amount of these components, polyurethanes with very different physical properties can be obtained. The component of diisocyanate is available in a wide range of compositions; only a few are of commercial interest. The most important types of diisocyanates for industrial use are 2,4- and 2,6-toluene diisocyanate (TDI) and 4,4′-diphenylmethane diisocyanate (MDI), each with different advantages and disadvantages. In general, TDI has the disadvantage of being a toxic compound due to the high volatility and chemical reactivity; MDI, being much less volatile, has a reduced toxicity in comparison with TDI. In contrast, the nonaromatic diisocyanates are seldom used for commercial applications compared to their aromatic counterparts, although they exhibit excellent resistance to light. (The products do not turn yellow like those containing aromatic diisocyanates.) The polyols used for polyurethane elastomers usually consist of two classes: polyethers or polyesters,[5] with molecular weights ranging from 1000 to 4000 g/mol. The typical chain extenders used are short-chain aliphatic diamines such as ethylenediamine (this produces poly(urethane−urea), PUU) or diols such as butanediol (this produces polyurethane, PU).

On the basis of the above compositions, the formed PUU or PU chains comprise alternating hard and soft segments. These two segments intrinsically are generally incompatible; they tend to separate into small domains (so-called microphase domains). The degree of phase separation depends on the thermodynamic driving forces and the kinetic pathways during processing. The final morphology usually consists of many hard-segment-rich domains, with sizes ranging from tens to hundreds of angstroms, dispersed in the matrix of soft segments.[6−13] The use of soft segments that do not hydrogen bond can particularly facilitate the microphase separation.[14] The hard-segment structure also plays an important role in phase separation. For example, the increase in the segmental length of the hard segment can promote the phase separation.[15,16] An increase in the hard-segment content can also result in larger hard-segment domain sizes as well as higher hard-segment domain concentrations in the soft-segment matrix.[1,17]

---

* To whom correspondence should be addressed. E-mail: bhsiao@notes.cc.sunysb.edu; hw.siesler@uni-essen.de.

10.1021/ma0214456 CCC: $25.00

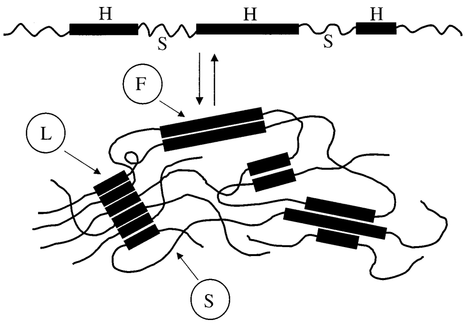

Figure 1. Schematic scheme of microphase separation in a polyurethane elastomer (H, hard segment; S, soft segment; F, fibrillar hard segment; L, lamellar hard segment).

In general, there are two different types of dispersed hard-segment morphologies present in segmental PUs/PUUs when the concentration of hard-segment is low: (1) fibrillar domains in which the domain axes coincide with the polymer chain axes, and (2) the lamellar domains in which the domain axes are perpendicular to the polymer chain axes (Figure 1).[18] These hard-segment domains connect the linear polymer chains in both the lateral direction and the chain direction, producing an effective cross-linking network that is responsible for the elastic properties of the polymer. Each microphase domain behaves as a cross-link junction that can be reversibly formed or destroyed by heat or solvation. Very often, these processes also cause the primary chains to permanently degrade.

The mechanical properties of polyurethanes are of great importance to their applications. Polyurethane elastomers can be stretched to many times the initial length and can retract back to almost the original shape and dimension. During deformation, the stress−strain curves under the stretching and recovery paths are different, which is termed the hysteresis. The area of the hysteresis curve is called the stress hysteresis and is related to the energy dissipated within the stretching and recovery cycle. Enderle et al. found that the area of the hysteresis depended on the strain rate, and larger deformational energies were required for higher stretching rates.[19] In the case of rapid cyclic elongations of an elastomer with a large stress hysteresis, the dissipation of the energy produced heat, which could result in deterioration of the sample. During the cyclic elongation and recovery processes of polyurethane elastomers, a large stress hysteresis is often seen in the first cycle. Although further repeated cycles can almost reach the same strain level, the subsequent process always generates a lower stress value than the one before. Bonart et al. observed that the second elongation process produced a higher stress than the relaxation process of the previous cycle; they concluded that this behavior was due to the breaking and partial reconstruction of hard-segment domains upon elongation and recovery.[18] The remaining strain value after the recovery of the sample represented the permanent deformation of the hard-segment domains.

Numerous studies have been carried out to study the structural development during deformation of polyurethanes.[10,11,20−27] In summary, the two types of hard-segment domain morphology—fibrillar and lamellar—can influence the deformation mechanism of the material in a very different manner.[18] As the long soft segments in the polymer chains are in the state of a random coil, the resulting matrix can be considered as a continuum. During deformation the hard-segment domains will initially be orientated by a continuum mechanical transfer of stress, initially tending to rotate their long axes parallel with the stretching direction. However, the exact deformation pathways of the hard-segment domains depend on their morphology and other physical properties. In the fibrillar morphology, the long axis of the domain is parallel to the chain direction. These domains can be easily oriented along the direction of chain extension (so-called positive orientation). In the lamellar morphology, as the hard-segment domain has its long axis perpendicular to the chain axis, the stretching process will initially begin to rotate the chain axes perpendicular to the chain extension direction (so-called negative orientation). These two mechanisms are illustrated in Figure 2.[18,20,28,29] In the initial stage of deformation, rotation of the lamellae dominates (the strain is usually less than 200%). At larger elongation strains, the stress transfer can lead to the destruction of lamellar hard-segment domains. The lamellar microdomains can break into smaller fragments of hard-segment aggregates with their long axes oriented perpendicular to the chain direction. However, sometimes the orientation behavior of some hard segments was found not to be completely consistent with the above mechanisms at high strains, suggesting that other mechanisms should also be considered.[30] For example, according to the work by Khranovskii et al.,[31] the inversion of orientation was not related to the destruction of the lamellar hard-segment domains but due to conformational transitions of the hard segments. These issues will be examined carefully in this work.

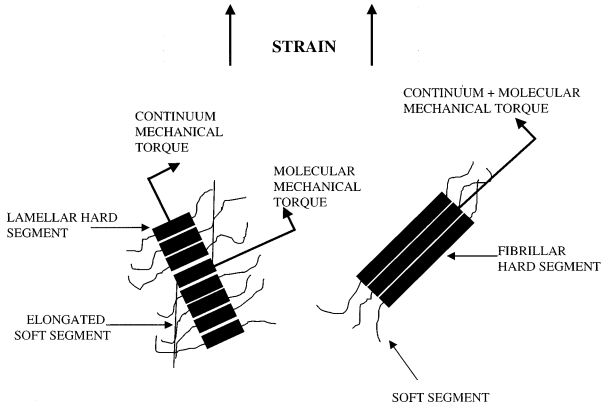

Figure 2. Bonart's model of orientation in a segmented polyurethane block copolymer. (For simplicity, the hard segments have been drawn of equal length for the lamellar and fibrillar hard-segment domains in this schematic representation.)

To study the in-situ structural changes during deformation and flow, one of the most powerful tools is the technique of rheooptics. The general principle of the rheooptics technique is quite simple. It involves the use of a mechanical testing method (such as the tensile method for solid or the rheological method for liquid) in combination with complementary optical measurements that can detect the structural information at the molecular level (birefringence, FTIR/FTNIR spectroscopy, Raman spectroscopy, small-angle X-ray scattering (SAXS), wide-angle X-ray diffraction (WAXD)). Such a technique can yield simultaneous results of bulk properties during deformation such as stress, strain, and strain rate and corresponding local structural parameters such as molecular orientation, crystallinity, domain morphology, and chain conformation.[32−34] The SAXS[10,11,35−42]

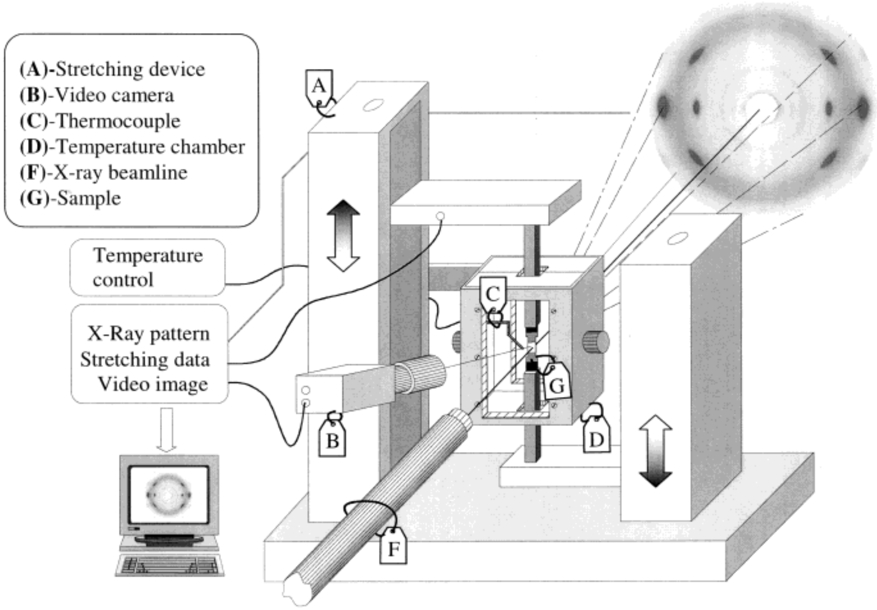

Figure 3. Schematic diagram of stretching apparatus (with temperature control chamber) setup for in-situ X-ray study.

and spectroscopy[6,8,9,22,43−48] techniques have been particularly useful to characterize the structure and morphology changes in PUs, PUUs, and thermoplastic elastomers under deformation.

In the present study, simultaneous SAXS/WAXD techniques with synchrotron radiation and time-resolved FTIR polarization spectroscopy in combination with a tensile stretching apparatus were used to obtain mechanical and molecular information during cyclic deformation of a PUU elastomer in real time. The specific emphasis will be placed on two aspects of the structural changes during deformation: (1) the effects of applied strain on the orientation and the transition of hard and soft segments and (2) strain-induced crystallization of the soft segments. The chosen PUU elastomer has a structure similar to some typical segmented polyurethanes. The diamine linkages in the hard segments, however, enhance the process of microphase separation because of additional hydrogen bonding relative to diol-extended hard segments in polyurethanes.

Experimental Section

Materials. The poly(urethane−urea) (PUU) used in this study was synthesized using a procedure similar to that described by Sakurai et al.[49] In this procedure, 4,4′-diphenylmethane diisocyanate (MDI) was reacted with poly(tetramethylene oxide) (PTMeO, M_W = 1800 g/mol) to form the prepolymer with diisocyanate end caps, which was subsequently dissolved in *N*,*N*-dimethylacetamide (DMAc). 1,2-Ethylenediamine (EDA) and diethylamine (DEA) were added to the prepolymer solution, where EDA was the chain extender and DEA was the chain terminator. The number-average molecular weight (M_n) of the segmented polymer formed was about 60 000 g/mol. The soft segments thus included the sequences of PTMeO and the terminal MDI that attaches to PTMeO groups, and the hard segments included the sequences of MDI and EDA. The weight percentage of the hard segments (MDI and EDA) was about 12% for the PUU sample studied here.

Film Preparation. A 10% w/w solution of PUU in dimethylacetamide (DMAc) was used for sample preparation. The solution was first cast on roughened glass slides (in order to suppress interference fringes in the FTIR spectra) and left at 50 °C in a vacuum oven overnight. The samples were then stripped off by placing the glass slides in warm water. They were left in warm water for half an hour to eliminate residual solvent. Finally, the samples were dried at 50 °C in a vacuum oven for 5 h. The typical sample thickness for FTIR experiments was about 10−15 μm measured by a micrometer. Great caution was taken to trim the samples to form the dimensions of approximately 10 × 5 mm^2. Irregularities along the edges of the sample could cause an earlier rupture and were carefully avoided. The film preparation for X-ray measurements was quite similar to that for FTIR spectroscopy, except that a greater thickness (about 1.2 mm) of film was produced. The sample dimensions for the X-ray study was trimmed to 3.3 × 30 mm^2.

X-ray Measurements. In-situ tensile deformation studies using simultaneous small-angle X-ray scattering and wide-angle X-ray diffraction (SAXS/WAXD) techniques[50] were carried out at the Advanced Polymers beamline, X27C, National Synchrotron Light Source (NSLS), Brookhaven National Laboratory (BNL). In this facility, a three-pinhole SAXS collimation system was used to define the incident beam from a double multilayer monochromator. The X-ray wavelength used was 0.1307 nm. The beam size at the sample position was about 0.4 mm in diameter. The sample-to-detector distance was 1590 and 140 mm for SAXS and WAXD, respectively. Two Fujifilm imaging plates were used as the SAXS and WAXD detector, and a Fujifilm BAS2000 image scanner was used to digitize the scattering images. The WAXD imaging plate had a central opening, allowing the passage of the SAXS signals. The deformation of the PUU film was performed with a modified Instron 4442 tensile apparatus. The stretching was carried out in a symmetrical mode, where the detection spot on the sample remained fixed. A schematic diagram of the stretching apparatus is shown in Figure 3. A constant strain rate was applied to the specimen throughout the deformation process. The SAXS/WAXD images were taken immediately after the desired strain values were reached during either the deformation or the relaxation process.

For the evaluation of orientation of the strain-induced crystals in the soft segments, the azimuthal intensity distribution $I(\phi)$ at $2\theta = 19.7°$ (at 0.1542 nm wavelength, if Cu Kα radiation was used) was analyzed. This peak represented the 110 reflection of the PTMeO crystals, which appeared on the equator during stretching. The Herman's orientation function f_x (where x denotes X-ray) can be calculated using the following equations:

$$f_x = \frac{3\langle \cos^2 \phi \rangle - 1}{2} \qquad (1)$$

with

$$\langle \cos^2 \phi \rangle = \frac{\int_{0°}^{90°} I(\phi) \sin \phi \cos^2 \phi \, d\phi}{\int_{0°}^{90°} I(\phi) \sin \phi \, d\phi} \qquad (2)$$

where ϕ is the azimuthal angle, being zero at the meridian and 90° at the equator. The orientation function calculated this way represents the degree of orientation along the stretching direction, being unity for perfect orientation and zero for no orientation.

FTIR Spectroscopy. The principal scheme of rheooptical FTIR/FTNIR spectroscopy measurements is illustrated in Figure 4a. A film sample under investigation was uniaxially drawn and recovered in a miniaturized stretching machine, which was modified to fit in the sample compartment of the spectrometer. During deformation, 12-scan interferograms were acquired in small time intervals (9 s) with polarized radiation alternately changed between the parallel and perpendicular directions with respect to the machine axis. Upon completion of the experiment, the interferograms were transformed to the corresponding spectra with a spectral resolution of 4 cm^{-1} for further process and analysis of the data. In the final analysis, the simultaneously obtained spectroscopic and mechanical data allowed the correlation of microscopic and macroscopic changes to be established. The schematic diagram of the electromechanical apparatus constructed for the rheooptical FTIR measurements is shown in Figure 4b. The implementation of a heating and cooling cell further offers the possibility to study deformation and stress−relaxation of polymers under controlled temperature conditions (±1.0 °C) from −50 to 200 °C.

The large number of spectra acquired during the rheooptical FTIR experiment required the use of software for evaluation of specific structural parameters from the spectra series with alternating polarization direction. A brief description of the data analysis scheme used in the software is as follows. The obtained FTIR spectra series have been evaluated (a) in terms of the structural absorbance A_0 of specific absorption bands[22,51]

$$A_0 = \frac{A_{\parallel} + 2A_{\perp}}{3} \qquad (3)$$

and (b) with reference to the orientation functions f (corresponding to the parameter derived from X-ray measurements; see eq 1) of selected functionalities from their absorption intensities by taking into account parallel or perpendicular transition moments to the polymer chain axis:

$$f_{\parallel} = \frac{R - 1}{R + 2} \qquad (4)$$

$$f_{\perp} = -2\frac{R - 1}{R + 2} \qquad (5)$$

In the above equations, $A_{\parallel}$ represents the integral absorbance parallel to the stretching direction, $A_{\perp}$ represents the integral absorbance perpendicular to the stretching direction, and R is the dichroic ratio defined as $R = A_{\parallel}/A_{\perp}$. The structural absorbance is used directly to represent the intensity parameter because it eliminates the influence of changing orientation on the actual intensity of the absorption band. Changes in the sample thickness during deformation are compensated for by comparison against a suitable reference band. For a detailed discussion of the characterization of anisotropy in polymers by dichroic measurements, the readers are referred to the pertinent literature.[52]

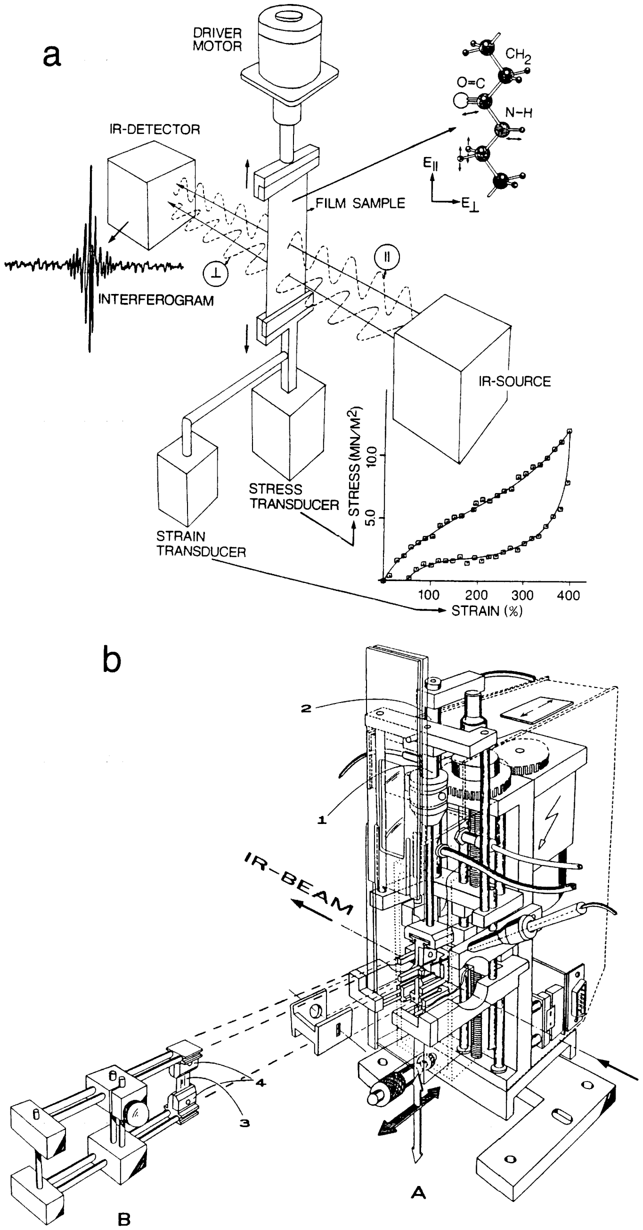

Figure 4. (a) Principle of rheooptical FTIR/FTNIR spectroscopy of polymer films. (b) Variable-temperature stretching machine for rheooptic FTIR/FTIR spectroscopy (A, stretching machine; B, sample preparation/transfer mechanism; 1, stress transducer; 2, strain transducer; 3, film sample; 4, sample clamps).

Results

WAXD/SAXS. The in-situ deformation study of the solvent-cast PUU film was carried out using simultaneous 2D-SAXS/WAXD methods with imaging plates. Figure 5 shows the selected 2D-WAXD images collected during deformation (strain = 0−700%). It is seen that the WAXD image at 0% is completely isotropic with an amorphous halo at about 4.5 Å in the initial state. However, a small sharp peak can be identified directly underneath the amorphous halo with a relatively narrower width. Since the melting point of the PTMeO crystal is around 10 °C, which is far below the measuring temperature (room temperature), we attribute this peak to the structure of the hard-segment domain, possibly due to the formation of a hydrogen-bonding plane by the urea groups of the hard segments.[53] Structural anisotropy in the WAXD image is seen immediately upon deformation (even in the first image collected at strain = 25%, not shown in the figure). The scattered intensity in WAXD is found to converge on

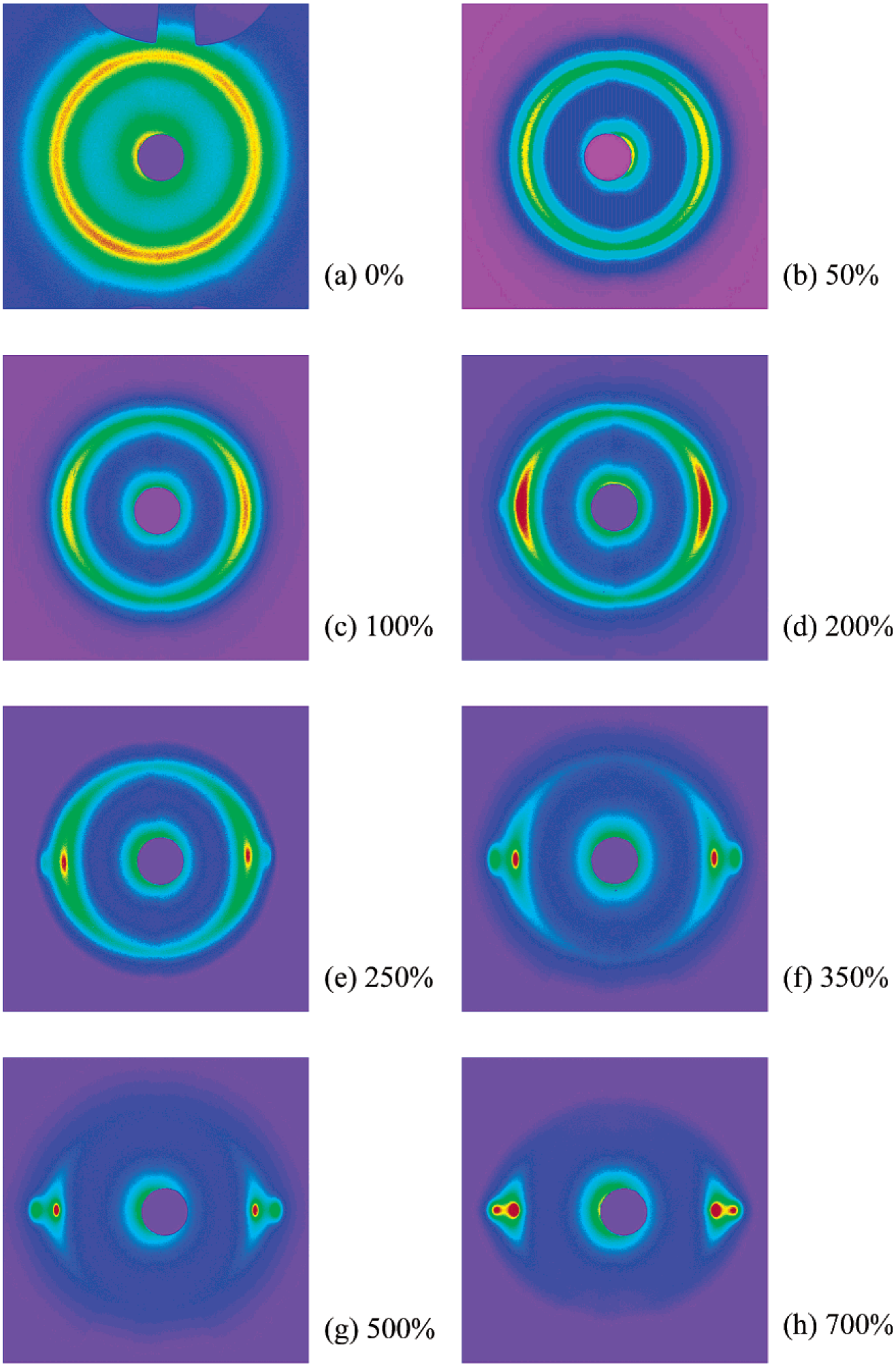

Figure 5. Selected WAXD patterns at different strains during deformation of PUU.

the equator with increasing strain, which indicates that the amorphous soft segment chains are gradually oriented along the stretching direction. At strain = 200%, the amorphous orientation is significantly increased, and two sharp crystalline diffraction peaks start to emerge on the equator. (One peak overlaps with the amorphous halo, and the other peak appears at a higher angle.) These two peaks are indicative of strain-

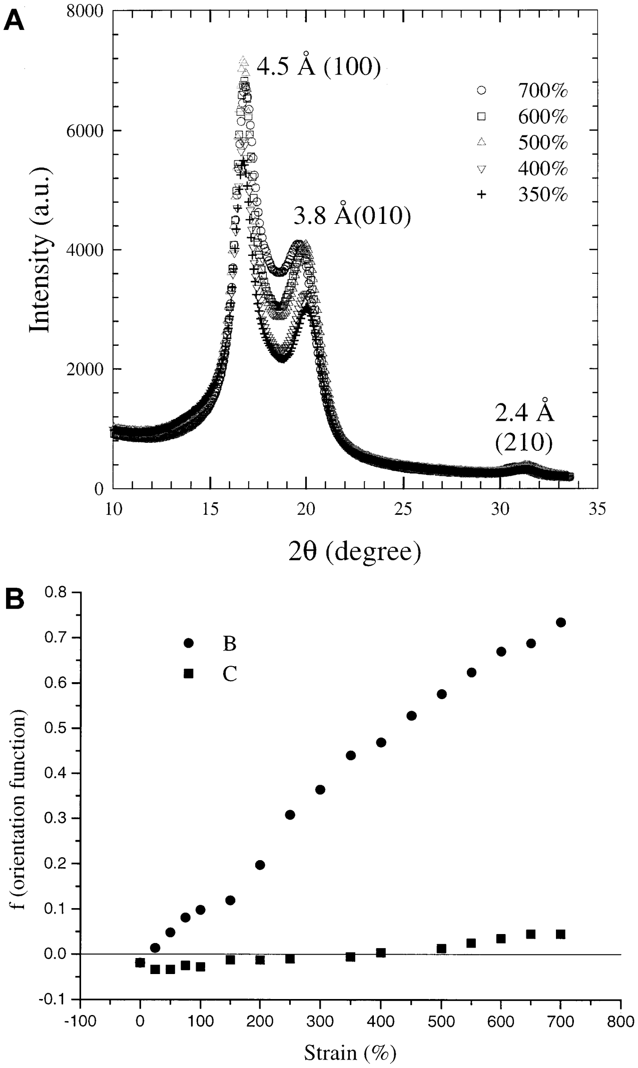

Figure 6. (a) Selected WAXD equatorial intensity profile; the two reflection peaks indicate the strain-induced crystallization of the soft segments. (b) Orientation function of strain-induced soft-segment crystals of poly(urethane−urea) derived from the azimuthal scan of WAXS at $2\theta = 16.8°$ (B, during stretching; C, after relaxation).

induced crystallization of the soft segments (PTMeO). With the increase of strain (up to 700%), the crystalline features become stronger and more oriented, whereas the unoriented amorphous phase becomes progressively weaker. In contrast, the peak from the hard segments was not affected by deformation. On the equator, the two strain-induced crystallization peaks appear first at strain = 200%. The lower angle peak also appears at about the same position as the weak scattering peak from the hard segments, but it is very strong and dominates the scattered intensity. The weak scattering peak can still be observed on the meridian even as the strain increases to 500%. At strain = 550%, this hard-segment peak completely disappears, and only a single amorphous peak (in a Gaussian function) is seen on the meridian. The equatorial intensity profiles from WAXD patterns at high strains are shown in Figure 6a, where three distinct reflection peaks are seen. These peaks result from the strain-induced PTMeO crystals with the following indices. The peak at 4.5 Å can be indexed as the 100 reflection, representing the interplanar spacing; the peak at 3.8 Å can be indexed as 010, and the peak at 2.4 Å can be indexed as 210.[10]

WAXD images were also taken upon relaxation after each strain (not shown here). All images of the recovered samples are found to be very similar to the one taken at the initial state (strain = 0%). This suggests that strain-induced soft segment crystals melt away at room temperature as soon as the stress is removed. Figure 6b illustrates the Herman's orientation function f_x calculated at the position of the 100 reflection, which also overlaps with the amorphous peak as well as the scattering peak from the hard segments. The value of f_x is found to increase continuously with strain (solid dot: B), but it returns to a near zero value at the relaxed state, i.e., isotropic (solid square: C). The hard-segment diffraction peak also recovers at the relaxed state from the stretching measurements. The slight increase in f_x at the relaxed state against the applied strain suggests that some structural changes by deformation are non-reversible, which is probably due to a slight degree of permanent change in the PUU film. This nonreversibility has also been observed in the SAXS results.

Selected 2D SAXS images during deformation at different strains are shown in Figure 7. The SAXS images acquired after relaxing the stretched film to zero stress from preset strains are illustrated in Figure 8. The isotropic peak of the SAXS image in Figure 7 represents the typical long-range correlation of the hard-segment domains due to microphase separation in PUs or PUUs.[10,54] The electron density difference between the hard and soft segments provides excellent contrast for SAXS. At the initial state (no stress), the isotropic SAXS image indicates that the hard-segment domains are randomly oriented. Under deformation, the SAXS images show dramatic changes. At strain = 25%, the SAXS image exhibits a four-point pattern, which can be attributed to the formation of tilted hard segments along the stretching direction. As the strain increases from 25% to 150%, there is little observable scattered intensity on the equator. This indicates that the hard-segment domains become uncorrelated in the direction transverse to the stretch direction.

At strain = 200%, the four-point SAXS pattern changes into two arcs on the meridian, along with a strong scattering streak on the equator. The equatorial streak represents the random correlation of some scattering objects highly oriented in the strain direction, which are consistent with the formation of strain-induced nanofibrils.[10,55] (We note that the strain-induced nanofibrils are quite different from the fibrillar domain morphology of the hard segments.) The two arcs represent the elongated hard-segment domains with some degrees of misorientation. At strain ≥ 300%, the SAXS image changes into two lobes on the meridian and a strong streak on the equator. The two-lobe pattern indicates that the stacks of hard-segment domains become oriented in the strain direction. Finally, when the strain becomes greater than 600%, the lobes and the streak diminish significantly, indicating that the lamellae are being destroyed. During the relaxation measurements, it is seen that after very high strains the microphase domain structures can be permanently changed (Figure 8). For example, at strains lower than 100%, the SAXS image collected after relaxation is the same as the image taken at the initial state. This indicates that the structure is completely recovered. In contrast, when the applied strain is around 600−700%, the SAXS image of the recovered specimen exhibits very

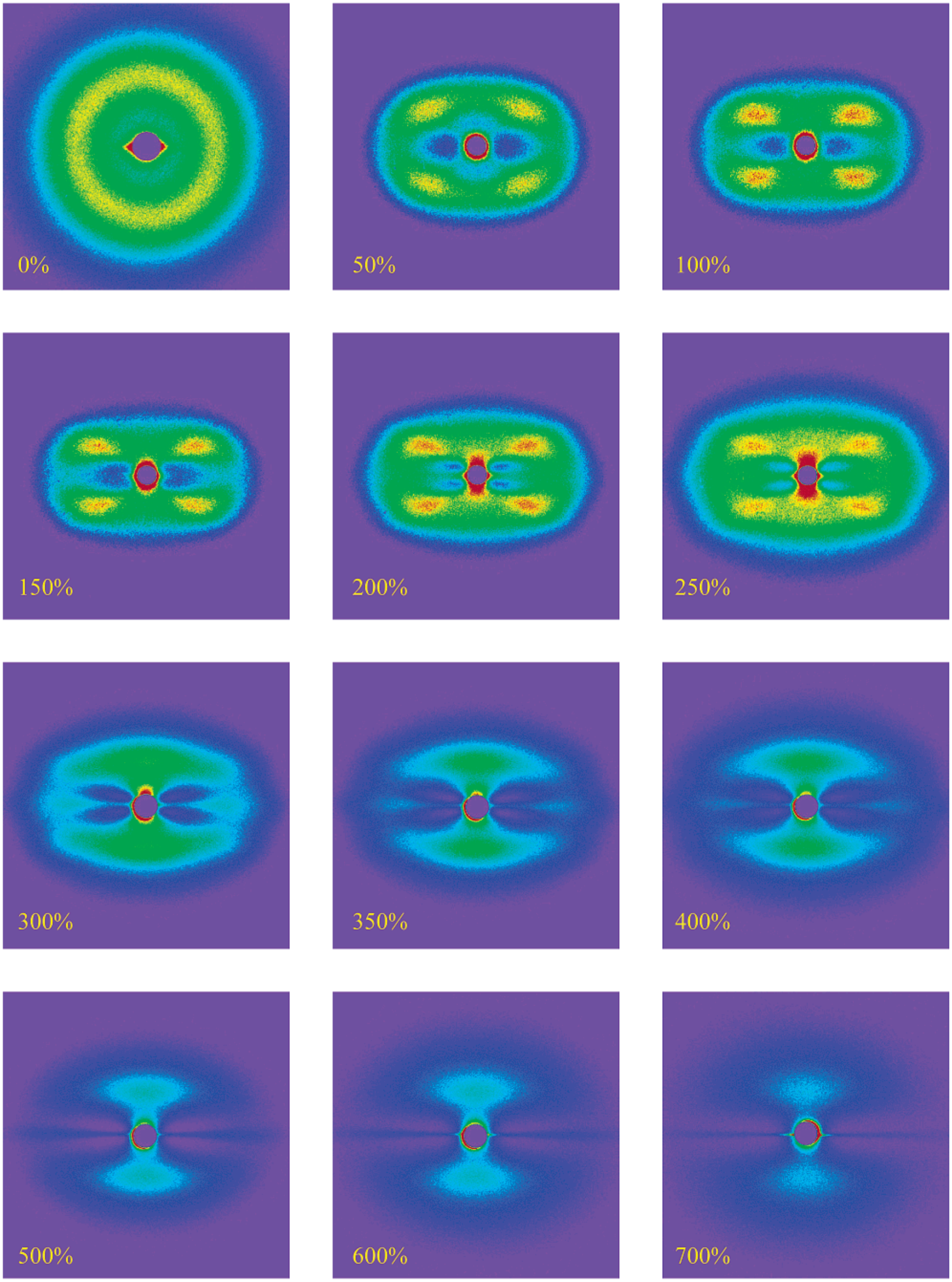

Figure 7. Selected SAXS patterns at different strains during deformation of PUU.

low intensity as compared to those relaxed from lower strains. This indicates a large degree of permanent hard-segment domain breakup at high deformation strains. Here, we must point out the above observed morphological changes are probably only limited in PUU where the hard-segment concentration is low.

FTIR. The PUU elastomer is particularly suitable for the rheo-FTIR study because the polymer contains

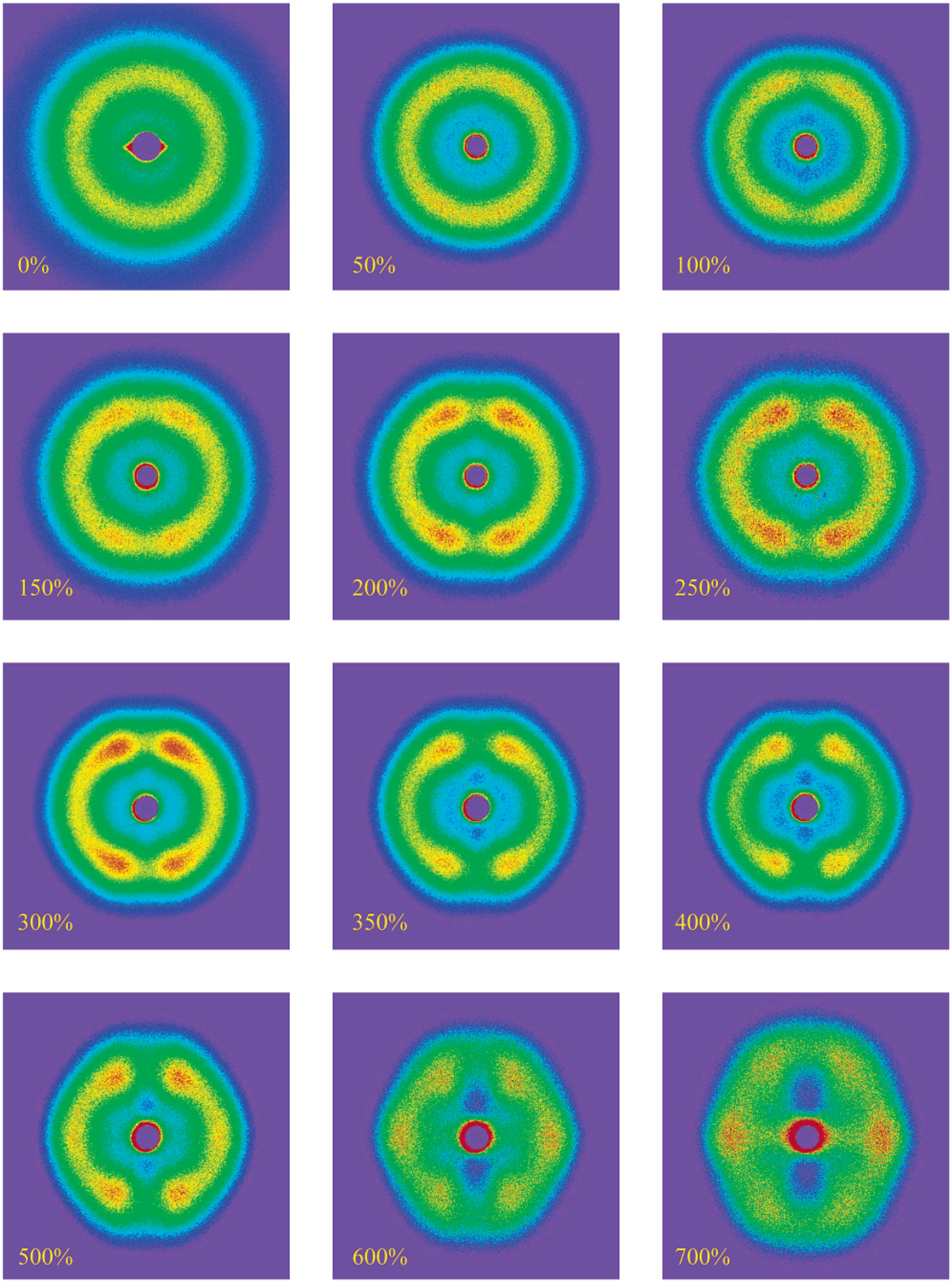

Figure 8. Selected SAXS patterns of the relaxed sample after relaxation of different applied strains.

functional groups with characteristic IR absorption bands, which can be assigned to specific locations in the microdomains. FTIR polarization spectra of this elastomer taken with radiation alternately polarized parallel and perpendicular to the stretching direction during a rheooptical elongation−recovery experiment up to 600% strain are shown in Figure 9 and clearly illustrate the dichroic effects as a consequence of the increasing

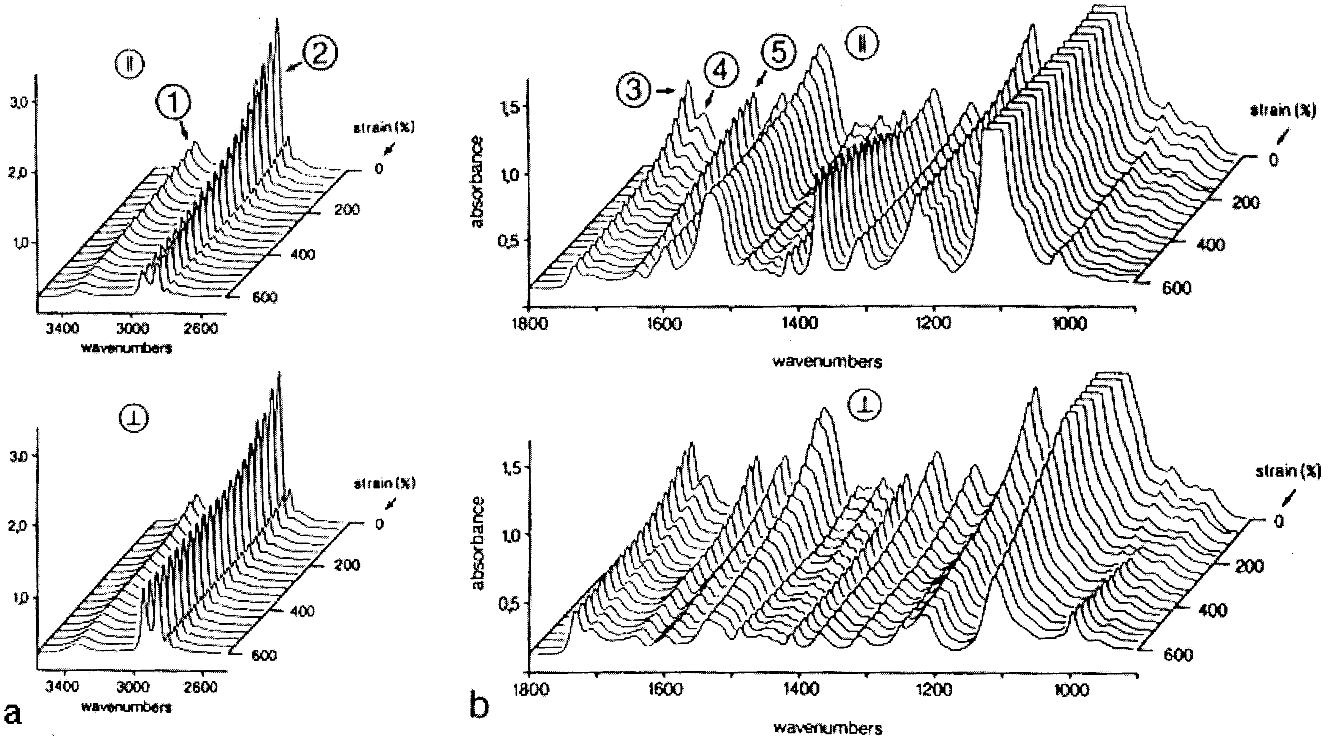

Figure 9. FTIR polarization spectra (top diagram represents $A_{\parallel}$; bottom diagram represents $A_{\perp}$) of poly(urethane−urea) taken during elongation up to 600% strain in the 3500−2500 cm^{-1} (a) and 1800−900 cm^{-1} (b) regions (1, ν(NH); 2, $\nu(CH_2)$; 3, free ν(C=O) urethane; 4, associated ν(C=O) urethane; 5, ν(C=O)-urea).

Table 1. Assignments of the Major Infrared Modes of a Poly(ether−urethane−urea) (Nakayama et al.,[56] Coleman et al.[57])[a]

wavenumber (cm^{-1})	assignments	int	polarization
3440	free ν(NH)	w	σ
3320	H-bonded ν(NH)	m	σ
2939	$\nu_a(CH_2)$	s	σ
2857	$\nu_s(CH_2)$	s	σ
2794	$\nu_s(CH_2)$	m	σ
1730	free ν(C=O) urethane amide I	m	σ
1710	H-bonded ν(C=O) urethane amide I	m	σ
1635	ν(C=O) urea amide I	m	σ
1592	ν(C−C) aromatic	m	π
1535	H-bonded ν(C−N) + δ(N−H) amide II	m	π
1527	free ν(C−N) + δ(N−H) amide II	w	π
1514	ν(C−C) aromatic	w	π
1410	ν(C−C) aromatic	w	π
1370	ω(C−H) in CH_2	m	π
1220	ν(C−N) + δ(N−H) amide III	s	π
1113	ν(C−O−C)	s	π
996	ν(C−O−C)	m	π

[a] s = strong, m = medium, w = weak, σ = perpendicular dichroism, π = parallel dichroism, subscript a = antisymmetric, and subscript s = symmetric.

anisotropy. The corresponding band assignments are summarized in Table 1.[56,57] The carbonyl region (1800−1600 cm^{-1}) in the FTIR spectra is most useful for the analysis of the hydrogen-bonding properties. The fraction of the hydrogen-bonded carbonyls, which is characterized by the hard−hard segment hydrogen bond (NH- - -O=C), can be used as a measure of the extent of microphase separation.

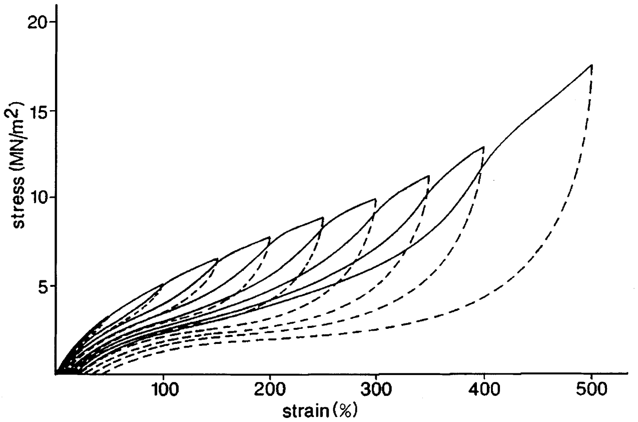

Figure 10. Stress−strain diagram of the investigated poly(urethane−urea) in successive loading (solid line)−unloading (dashed line) cycles increasing by 50% strain intervals up to 500% strain.

In the deformation study, the samples were typically subjected to successive elongation−recovery cycles with a strain and recovery rate of 115% per minute, increasing by 50% strain intervals up to 500% strain (Figure 10). The observed stress−strain envelope during deformation is identical to the corresponding stress−strain curve of a continuous elongation−recovery process to the maximum elongation. The observed relationship reflects substantial irreversible effects and an increase in hysteresis with increasing elongation strain.

Owing to their almost uncoupled nature and separate frequency positions, the $\nu(CH_2)$ (3000−2700 cm^{-1}), ν(NH) (3320 cm^{-1}), and ν(C=O) urea (1636 cm^{-1}) absorption bands can be utilized for the characterization of soft-segment (CH_2) and hard-segment (NH, C=O) orientation. It has to be kept in mind, however, that the $\nu(CH_2)$ vibration is overlapped by the absorption contributions of the diphenylmethane and the ethylenediamine units and that the ν(NH) absorption stems from equal parts from urea moieties and urethane units (isolated or incorporated in hard segments). Additionally, it can be derived from the ν(NH) band that the majority of the NH groups are hydrogen-bonded. The transition moment angles of these vibrations have been taken as 90° with reference to the local chain axes, although it is recognized that some deviation from this value may occur for the ν(CH_2) and ν(C=O) vibrations due to superposition with the corresponding (CH_2) wagging mode and as a consequence of strong mechanical and electrical coupling of the (C=O) and (C−N) stretching vibrations, respectively. It should be mentioned, however, that these slight deviations will not significantly influence the values of the calculated orientation functions. In view of the small length-to-width ratio of only 2, we have tested uniaxiality by verifying the invariance of the dichroism of an elongated sample with the IR beam impinging perpendicular to the film plane and after rotating the film for 45° around the stretching direction. Based on the hard-segment crystal structure proposed by Blackwell et al.[58] and Hespe et al.[59] from the study of model compounds, the orientation functions of the hard-segment absorptions cannot take on the maximum theoretical positive value of 1.0. (An orientation function value 1.0 is obtained only for a perfectly elongated chain.) In an attempt to accentuate absorption bands which can be assigned to the strain-induced crystal phase, absorbance subtraction of the spectrum of an undrawn specimen from the spectrum of a 600% elongated sample revealed that several absorption bands have increased in relative intensity during elongation despite a substantial reduction of sample thickness (Figure 11). From a closer inspection of their wavenumber positions, these absorption bands can be assigned to conformational regularity bands of crystalline PTMeO segments.[60] Hence, the spectra measured on-line to the mechanical treatment also allow monitoring of strain-induced crystallization of the soft segments.

In Figure 12 the orientation functions of the ν(CH_2), ν(NH), and the ν(C=O) urea absorptions have been plotted versus strain. Integral absorption intensities have been utilized for the calculation of the orientation functions of the various functionalities. The soft-segment orientation is predominantly represented by the CH_2 groups in the polyether and shows in all cycles an almost linear increase of positive orientation as a function of elongation and a reversible disorientation upon recovery. A completely different behavior is reflected by the orientation function/strain dependence of the urea−carbonyl absorption, which represents the lamellar and fibrillar hard segments although fibrillar domains are probably only present at finite strains. Throughout the mechanical treatment, a distinct transverse orientation can be observed. Up to the third elongation−recovery cycle (maximum elongation 150%), this transverse orientation is reversible upon recovery. This observation is also supported by a comparatively small hysteresis in the stress−strain diagrams up to this degree of elongation (Figure 10). As soon as the maximum elongation exceeds this strain value of about 150%, the orientation function runs through a minimum before the maximum elongation of the corresponding cycle is reached and reverses toward positive orientation. This behavior can readily be explained with the fragmentation of negatively oriented lamellar domains into smaller fibrillar units, which then orient with their long axes (which coincide with the polymer chain axes) in the direction of elongation. The minimum in the course of the orientation function indicates the strain value where a further increase in transverse orientation is compensated by the positive alignment of the smaller fragmental fibrillar domains. Because of the incomplete restoration of the original structure and partial reorganizations, the minimum in the transverse orientation becomes less significant at increasing strain cycles. At higher elongation levels, the ν(C=O) urea orientation function even increases beyond the zero value of the orientation function during recovery. This effect can be attributed to the entropy-driven relaxation of the soft segments in the unloading process. As the soft segments relax, they impose a barrier to the recovery of the increasingly disrupted hard segments and exert an additional orientating tension. The ν(NH) orientation

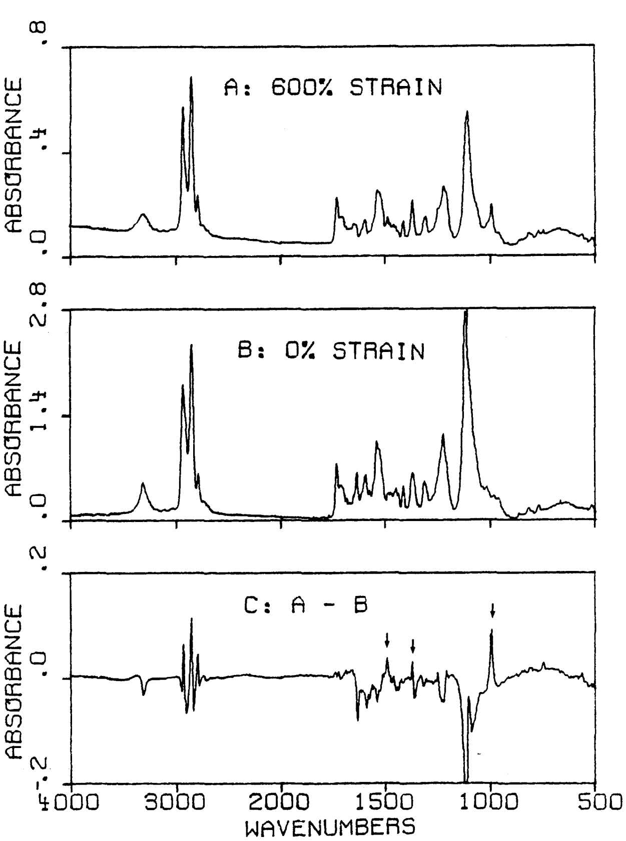

Figure 11. Accentuation of strain-induced crystallinity in the structural absorbance spectra of the investigated PUU: (a) 600% drawn sample; (b) undrawn sample; (c) difference spectrum (a) − (b) (↓: indicates the conformational regularity bands of the polyether segments).

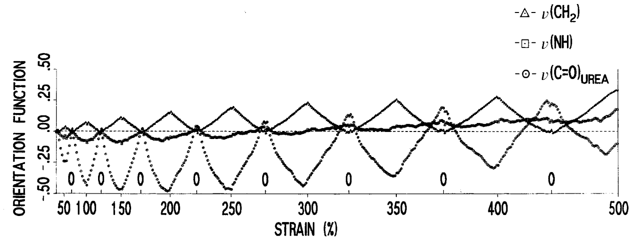

Figure 12. Orientation function/strain plots of different absorption bands of the PUU under examination. (upper curve, ν(CH_2); center curve, ν(NH); lower curve, ν(C=O) urea).

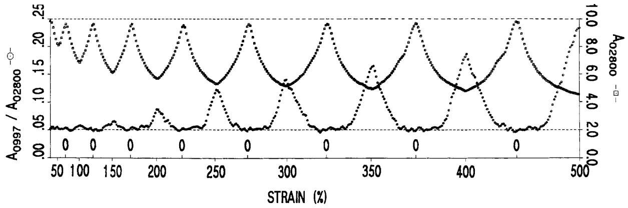

Figure 13. Characterization of strain-induced crystallization of the soft segments and thickness variation of the investigated PUU at 300 K (upper curve, A_{o2800}; lower curve, A_{o997}/A_{o2800}).

function, on the other hand, exhibits a behavior which lies in between the extremes of hard- and soft-segment orientation because it represents not only the urea groups, which are primarily located in the hard segments, but also the urethane functionalities, which are partly located in the hard-segment boundary and partly occur as isolated units in the soft-segment matrix. Because of the compensation of positive and negative orientation effects, the minimum in the ν(NH)-orientation function/strain-curve extends to less negative values during the initial elongation−recovery cycles compared to the urea functionality and moves toward positive values at higher elongations with rather small changes as a function of strain.

The possibility to monitor strain-induced crystallization in the soft-segment phase of the investigated PUU is demonstrated in Figure 13. Here, the integral structural absorbance ratio of the conformational regularity band and the thickness reference band has been plotted alongside the intensity of the reference band versus strain. Basically, the graph demonstrates the reversibility of the thickness changes and the strain-induced crystallization as a function of cyclic loading−unloading. We note that one can distinguish strain-induced soft segment crystals versus oriented but noncrystalline soft segments by FTIR. In this study, the chosen absorption band for monitoring the strain-induced crystallinity is a crystallinity-sensitive band in PTMeO, which is independent of the changes in oriented noncrystalline soft segments. As a consequence of the disruption of the lamellar hard-segment structure, the onset of crystallization is gradually shifted to higher strain values with increasing number of cycles.

Discussion

It is well-known that segmented PUUs have microdomain structures due to the phase segregation of two different building blocks. In the hard-segment domain, the hydrogen bonding between urea C═O and NH functionalities plays an important role to stabilize the structures. These microdomains behave as physical cross-links in the material.[10] Although some studies reported that the hard segments can crystallize,[54,61] the crystalline diffraction peaks are difficult to detect by WAXD in this study because of the low volume fraction and low degree of lateral perfection in the crystals (see Figure 5). However, the effects of hard-segment crystallization on the elastic properties have been well documented. For example, Bonart et al. studied the crystal structure in selected PUU samples.[10] Wang and Cooper investigated the effects of the hard-segment content on the morphological, mechanical, and physical properties of PUU.[54]

The SAXS image taken from the as-cast sample shows that microphase domains are randomly oriented with very strong scattered intensity (Figure 7). Considering the relatively low volume fraction of the hard segments in this PUU sample, we conclude that the degree of phase separation is relatively complete through solvent casting.[54] In PUs, it is known that some short hard segments are dissolved in the soft-segment matrix,[17,21] due to the hydrogen bonding between the N−H group and oxygen in the ether linkage as well as the kinetic restrictions limiting the hard segments to segregate. Typically, the phase separation of PUU is better than that of PU at the equivalent hard-segment content and block length. This is because the aromatic polyurea groups possess strong hydrogen-bonding capability, which significantly stabilize the hard-segment domain. Only at low concentrations and/or short block lengths, the formation of the hard-segment domains containing polyureas can be retarded. The role of the urea linkage in the hard-segment domain has been studied by Sung et al.,[62] who reported that a single N−H group could be bonded to two urea carbonyls in a nonplanar three-dimensional configuration. It was also reported by Wang and Cooper that the interface between the hard domain and the soft matrix in PUU was very sharp, as most of the urethane carbonyls were non-hydrogen-bonded.[54] However, Runt et al.[63] recently reported that the degree of phase separation from a series of PUUs with different hard-segment contents was not complete as suggested by earlier studies.[54,62] A large degree of phase mixing was calculated from analysis of small-angle X-ray scattering data.

Soft-Segment Orientation. WAXD results indicate that all soft segments are in the noncrystalline state in the undeformed PUU sample. Cooper et al. reported that the radius of gyration of polyether soft segments in PU was substantially larger than that of polyether homopolymer in the θ solvent. This suggests that the soft-segment chains in PU are in a relatively "extended" conformation,[64] which facilitates the stress transfer to the neighboring hard-segment domains. However, as the distributions of the soft-segment chain length and the hard-segment domain size are quite large, stress cannot be homogeneously dispatched in the soft segments during deformation. Consequently, a stress distribution around each domain can be generated, leading to a torque to reorient the hard domains and to minimize the local stress. Such a mechanism is supported by our WAXD/SAXS observations. For instance, WAXD images showed a relatively small increase in orientation of the amorphous phase (dominated by the soft segments) in the strain region between 25% and 150% (f increases only from 0 to 0.1 in Figure 6a). In contrast, the corresponding orientation changes in the SAXS patterns are substantial. These changes are primarily due to the antiparallel orientation of the hard-segment domains by low strains. At strains > 200%, WAXD results indicate that strain-induced crystallization in soft segments occurs. Although the amount of the crystals produced is initially low, the resulting orientation of the crystals is high. This is evident by the appearance of two sharp diffraction peaks on the equator, overlapping with the less oriented arc from the amorphous phase (Figure 6). These highly oriented crystals probably consist of the extended chain morphology; the folded chain crystallization will not be energetically favorable to occur under the deformation conditions. At strains above 250%, the fraction of the induced crystals increases. This is seen by the sharp increase of the diffraction intensity corresponding to the two crystalline peaks at the expense of the amorphous scattering. At strain = 600%, we can only detect a trace amount of amorphous phase from the soft segments.

The WAXD observations are in good agreement with the in-situ FTIR results. For example, from the absorbance ratio of the conformational-regularity band shown in Figure 13, it is clear that strain-induced crystallization begins to appear at strains above 150%. This absorbance ratio not only increases with increasing strain, but it returns to the initial value under complete relaxation, indicating the disappearance of the strain-induced crystallites upon recovery.

Finally, we assert that the strain-induced crystals of soft segments become partial load-bearing species in PUU under deformation, which form the base for formation of microfibrils or nanofibrils.[10,55,65] (Again, we point out the difference between nanofibrils, which consist of soft-segment crystals and the fibrillar hard-segment domains illustrated in Figures 1 and 2.) The hard segments within the nanofibrils are also oriented with chains aligned parallel to the machine direction at high strains. The observed strain hysteresis properties in PUU thus are attributed to several convoluted mechanisms involving the breakup of hard-segment lamellae, the formation of load-bearing nanofibrils,[10,55,65] their progression, breakdown, and re-formation with cyclic variation of strain.

Hard-Segment Orientation. Bonart provided the first systematic studies of morphological changes during deformation of segmented PUs.[10] He concluded that the orientation of the hard segments depended on the level of the strain applied and the change of the hard-domain morphology and orientation with strain. We will elaborate on this point further here. In the current studied system, the hard-segment content is low and should form isolated domains randomly dispersed in the soft-segment matrix. As long as the soft segments are randomly coiled, the surrounding matrix can be regarded as a continuum. Under deformation, the hard-segment domains are reoriented by the mechanical transfer of stress from a continuum, and the long-axis dimension of these domains will be aligned along the direction of stretching. As a result, the hard segments in the nanofibrillar domains, in which the long axis coincides with the chain axis, will possess a positive orientation, whereas the hard segments in the lamellar domains, in which their long-axis is perpendicular to the chain axis, will possess a negative orientation assuming that the lamellae rotate with their long axes becoming parallel with the stress direction. Judging by the low concentration of the hard segments in the investigated PUU, we argue that the concentration of the fibrillar domains, which require a long hard-segment length, is low, and that the concentration of the lamellar domains is high. This has been recently verified by us using the AFM technique.[66] Thus, the SAXS pattern observed at the early stages of deformation is dominated by the lamellar morphology of the hard segments. However, in a system with higher hard-segment composition where more continuity of the hard-segment phase would exist, the morphological behavior during deformation might be different from current studies.

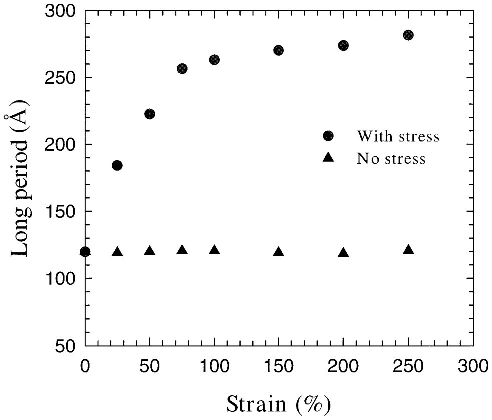

Figure 14. Interdomain spacing (L) change of the lamellar microstructures as a function of strain during and after deformation.

The interdomain spacing at the early stages of deformation has been calculated from Figure 7 using Bragg's law, and the results are shown in Figure 14. It is seen that the average spacing between the domains (L) increases sharply at the initial stages of deformation, prior to the occurrence of strain-induced crystallization of the soft segments (at strains < 150%). Even though the level of strain-induced soft-segment crystallization substantially increases in total volume fraction from 150% to 300% and beyond, the value of L plateaus at about 100%. Evidently, the degree of slip of chains and domains along with the microscopically heterogeneous stress contributes to this behavior. For example, one must consider the idea that many of the lamellae are under considerably lower stress than the highest stress regions. Strain-induced soft-segment crystals also become stress-bearing domains under deformation and could contribute to the plateau behavior. Upon relaxation, the interdomain spacing returns to the original value.

The unique evolution of the SAXS pattern reflects the changes in the hard-segment morphology. In Figure 7, a distinct four-point SAXS pattern is seen at strain = 50%, which indicates the tilting of the hard-segment domains. The observed SAXS scattering in the meridional direction gives values of L ranging from 100 to 300 Å. This is mainly due to the lamellar morphology of the hard-segment domains (the domain axis is perpendicular to the chain axes). However, the observed scattering patterns change significantly at high strains. The key SAXS features observed in Figure 7 and the possible morphological characteristics are summarized as follows. Qualitative schematics of domain orientation for the various strain levels are given in Figure 15. The following also describes the various contributions to the 2D SAXS patterns.

1. Strain = 0%. A circular scattering halo is seen, indicating that the morphology consists of hard-segment lamellar stacks (**A**) without preferred orientation. (Note the domain axes are perpendicular to the polymer chain axes in hard-segment lamellae as seen in Figure 1.)
2. Strain = 50%. A four-point pattern with teardrop-shaped scattering peaks oriented in the arc direction is seen, which suggests that both lamellae and stacks are tilted with respect to the stretching direction. (The hard segment is aligned perpendicular to the lamellae.) The long period is found to increase along the stretching direction due to the increased separation of hard-segment lamellae in the stacks.
3. Strain = 100−150%. A four-point pattern with diagonal orientation of teardrops is seen, which indicates the lamellar tilting persists but with a vertical orientation of the lamellar stacks in the stress direction.

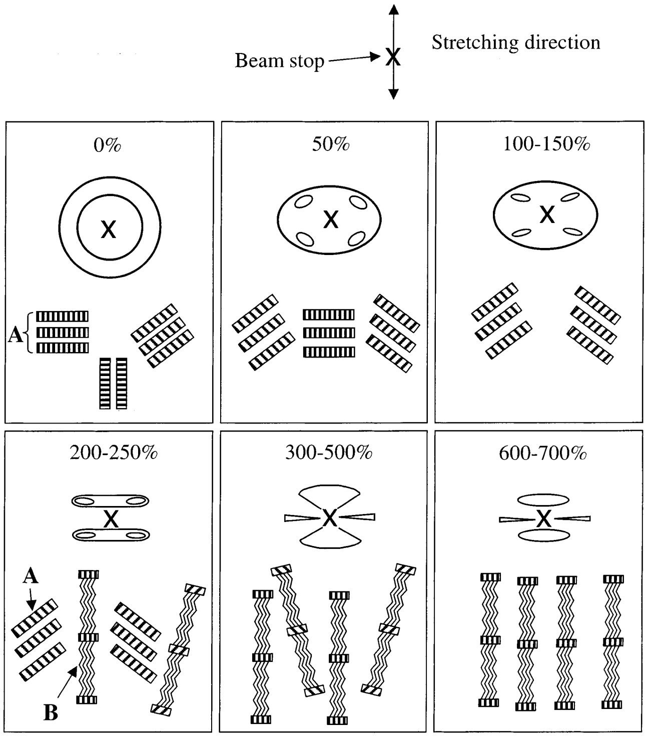

Figure 15. Schematic diagram illustrating the relationships between the morphology of hard-segment lamellar domains and the SAXS pattern (**A** represents the hard-segment lamellar microstructure; **B** represents the strain-induced nanofibril consisting of soft-segment crystals).

We note that the observed pattern also contains a superimposed scattering halo, indicating that some randomly orientated lamellae stacks are present.

4. Strain = 200−250%. Coalesced six-point pattern containing four diagonally oriented teardrops and a pair of weak broad scattering bars along the meridian (the stretching direction). The scattering halo in (3) disappears completely. The broad meridional two-bar pattern is consistent with a contribution from nanofibrils oriented parallel with the stress direction, where the lamellae are aligned perpendicular to the stretching direction but the hard and soft segments are aligned along the stretching direction. The superimposed four-point teardrop pattern indicates the presence of some remaining tilted lamellae. A loss of equatorial scattering indicates the lack of horizontal orientation of lamellar stacks.

5. Strain = 300−500%. Further breakdown of original lamellar stacks and formation/orientation of nanofibrils. In addition, an equatorial streak is seen, which is probably due to the density contrast between vertically oriented nanofibrils containing crystallized soft segments and broken down hard domains.

6. Strain = 600−700%. The appearance of the two-point pattern indicates better orientation of stacks with lamellae, which are broken down enough such that tilting becomes minimal. The population of highly oriented nanofibrils increases from 600 to 700%.

The above explanation of the scattering patterns can be elaborated on further as follows. In a paper emphasizing semicrystalline homopolymers, mathematical translations between real-space morphologies and two-dimensional reciprocal space patterns have been provided.[67] At low strains, the torque on the lamellar domains generated through the strained soft segments will cause the domains to rotate with a tendency to align the domain axis parallel to the stretching direction (Figures 2 and 15). At strains between 100 and 150%, the four-point pattern remains at similar positions but the orientation changes, transforming it into four diagonally oriented teardrops (Figure 15). This indicates that the stress is high enough causing the shear deformation of the lamellar domains, where the tilting of the majority of lamellae persists but the stacks of hard domains become parallel to the machine direction. At this stage, the network remains intact and the morphology is substantially reversible. Once the strain is released, many of the tilted domains return to their original state.

At strains between 200% and 250%, the SAXS pattern changes again with substantial infilling of the scattered intensity in the meridian between the off-axis scattering peaks (Figure 7). The occurrence of the scattered intensity along the meridional axis suggests that a fraction of the lamellar stacks becomes oriented in the stretching direction. It is conceivable that the hard-segment lamellae become shorter (less anisotropic) because of breakup of some domains at these higher strains. Substantial levels of tilted, mostly intact lamellae still exist because strong remnants of the four-point pattern are observed. With increases in strain above 200%, the strain-induced nanofibrils or force strands (load bearing soft segments connected by small hard-segment domains) must break down and re-form, presumably by chain slippage and breaking of hard domains. At the same time, new force strands are formed (some form crystallization), causing a large redistribution of stress. Notice that stress is heterogeneously distributed on a nanoscopic length scale.[10,55] Increasing levels of hard-segment chains become oriented in the direction parallel to the stretching direction because of the increasing population of force strands. Thus, we argue that different morphological changes prevail depending on the levels of the strains applied. At low strains, the lamellar domains tend to rotate in the direction parallel to the stretching direction because of the perpendicular orientation of hard domains in the nanofibrils. At intermediate strains, this is combined with domains that are broken down into smaller lateral sizes with the domain axis perpendicular to the machine direction but the chain axis parallel. At high strains, the parallel alignment of hard segments dominates because of formation of nanofibrils containing hard and soft blocks with a parallel chain orientation.

The increase in oriented nanofibrils (force strands) is attributed to the vertically oriented stacks of broken down lamellae separated by highly stressed and oriented soft segments (with a sizable fraction of crystallinity). The fraction of these lamellae forming the nanofibrils increases significantly at strains from 300% to 700%. However, the scattered intensity is found to be greatly reduced at these strains. There are two possibilities to explain the intensity decrease: (1) a decrease in population—some hard domains are broken down to sizes too small to contribute to coherent scattering—and (2) a decrease in contrast between the hard-segment domain and the surroundings—the increase in strain-induced soft-segment crystal populations decreases the contrast between the hard and soft domains. In Figure 7, the evidence of the strain-induced nanofibrils (at 300−500% strains) can be seen by the appearance of the equatorial streak (transverse scattering) detectable because of the high intensity of the synchrotron source. The occurrence of the scattering streak suggests that the adjacent strain-induced nanofibrils are not correlated as might be expected because of the uncorrelated nature of such regions of nonuniform stress. This type of transverse scattering has also been detected recently in highly oriented thermoplastic elastomers.[53] At high strains, the chain slippage and breaking of hard-segment domains causes a redistribution of stress, which is not reversible with relaxation of stress because of permanent hard-segment domain network deformation.

SAXS results are in good agreement with FTIR results, where the deformation mechanism includes hard-segment domain lamellar rotation which dominates up to about 200% strain and the maximum negative (perpendicular) chain orientation depends on the stability of the lamellar morphology and the length of the soft segments. For lamellar hard-segment domains, this mechanism leads to a disruption of the initially transversely oriented structural units into smaller, fibrillar domains with a subsequent positive orientation of the polymer chains into the stretching direction. In the case of fibrillar hard segments continuum- and molecular-mechanical transfer of stress both contribute to a positive alignment of the polymer chains. As the concentration of the fibrillar hard-segment domains is initially low, it does not contribute substantially to the observed SAXS pattern. The disruption and reorganization of the hard segments during the mechanical treatment also have an effect on the wavenumber position and the shape of the urea−carbonyl band as a function of the applied strain.[22] While the urethane−carbonyl absorptions retain their peak maximum wavenumber positions at 1732 and 1709 cm^{-1} throughout the loading procedure, a shift from 1637 to 1641 cm^{-1} and a concommitant broadening of the band shape can be detected for the urea−carbonyl absorption beyond the strain value, corresponding to the minimum of the $\nu(C{=}O)$ urea orientation function. These effects can be interpreted by a weakening of the hydrogen bonds and a broader distribution of their energies in the disrupted lamellar structure, respectively.

Conclusions

The segmental orientation of a poly(urethane−urea) elastomer containing low concentration of hard segment during cyclic elongation and recovery has been investigated by simultaneous mechanical and differential optical measurements, namely, wide-angle X-ray diffraction and small-angle X-ray scattering and time-resolved Fourier transform infrared spectroscopy. WAXD results show that the initially isotropically oriented soft segments increase in orientation with increasing strain. Stress-induced crystallization is detected and characterized by WAXD. Both the orientation and stress-induced crystallization are relaxed after releasing the applied stress, although some minor hysteresis was found for hard segments after high strains (>500%).

Both SAXS and FTIR results show that the tested PUU has very well phase-separated morphology. The interdomain spacing of as-cast PUU is 10.6 nm and increases with increasing strain and was restored to its initial value if relaxed from strains less than 250%. It is found that the hard-segment lamellae are sensitive to the applied stress and are tilted toward the stretching direction in the strain range of 25−150%. The isotropic distribution is fully restored after releasing stress with negligible permanent structural changes observed over this strain range. As the strain increases to 200−250%, the morphology contains tilted lamellae with hard segments becoming aligned parallel to the stretching direction. When strain is further increased to 300−500%, the hard-segment domains start to be broken down to smaller domain sizes but with higher orientation in the strain direction. At high strains, the formation of the equatorial streak in SAXS also indicates the formation of nanofibrils containing fragmented hard-segment domains and strain-induced soft-segment crystals, and the correlation of the highly oriented nanofibrils perpendicular to the strain direction is poor. The SAXS intensity is reduced at the highest strains of 600−700% as the results of less density contrast and other features related to the nanofibrillar morphology.

Acknowledgment. The authors acknowledge the technical support of this study by Prof. Benjamin Chu, Drs. Igors Sics, Dufei Fang, and Lizhi Liu. F.Y. and B.S.H. acknowledge the financial support of this work by a grant from the National Science Foundation (DMR-0098104). Synchrotron X-ray experiments were carried out at the Advanced Polymers Beamline at the National Synchrotron Light Source, Brookhaven National Laboratory, which is supported by the U.S. Department of Energy (DE-FG02-99ER 45760). H.W.S. acknowledges financial and instrumental support by the German Research Foundation, the Ministry of Research and Education, NRW, Germany, and the Research Pool of the University of Essen.

References and Notes

(1) Hepburn, C. *Polyurethane Elastomers*; Elsevier, Applied Science: Amsterdam, 1992.
(2) Legge, N. R., Holden, G., Schroeder, H. E., Eds.; *Thermoplastic Elastomers: A Comprehensive Review*; Hanser: Munich, 1987.
(3) Szycher, M. *Handbook of Polyurethanes*; CRC Press: Boca Raton, FL, 1999.
(4) Woods, G. *The ICI Polyurethanes Book*, 2nd ed.; Wiley: Chichester, UK, 1990.
(5) Kipphardt, H. Influence of the soft segment of thermoplastic polyurethane on final product properties. Polyurethane World Congress, Sept−Oct 1987; p 146.
(6) Estes, G. M.; Cooper, S. L.; Tobolsky, A. V. *J. Macromol. Sci., Rev. Macromol. Chem.* **1970**, *4*, 313.
(7) Cella, R. J. *J. Polym., Polym. Symp.* **1973**, *42*, 727.
(8) Lilaonitkul, A.; West, J.; Cooper, S. L. *J. Macromol. Sci., Phys.* **1976**, *12*, 563.
(9) Lilaonitkul, A.; Cooper, S. L. *Rubber Chem. Technol.* **1977**, *50*, 1.
(10) Bonart, R. *J. Macromol. Sci., Phys.* **1968**, *B2*, 115.
(11) Bonart, R.; Morbitzer, L.; Hentze, G. *J. Macromol. Sci., Phys.* **1969**, *B3*, 337.
(12) Koberstein, J. T.; Gancarz, I. *J. Polym. Sci., Polym. Phys.* **1986**, *24*, 2487.
(13) Lee, H. S.; Hsu, S. L. *Macromolecules* **1989**, *22*, 1100.
(14) Speckhard, T. A.; Hwang, K. K. S.; Yang, C. Z.; Laupan, W. R.; Cooper, S. L. *J. Macromol. Sci., Phys.* **1984**, *23*, 173.
(15) Fu, B.; Macknight, W. J.; Schneider, N. S. *Rubber Chem. Technol.* **1986**, *59*, 896.
(16) Meuse, C. W.; Yang, X.; Yang, D.; Hsu, S. L. *Macromolecules* **1992**, *25*, 925.
(17) Koberstein, J. T.; Galambos, A. F.; Leung, L. M. *Macromolecules* **1992**, *25*, 6195.
(18) Bonart, R.; Müller-Riederer, G. *Colloid Polym. Sci.* **1981**, *259*, 926.
(19) Enderle, H. F.; Kilian, H. G.; Hespe, H. *Colloid Polym. Sci.* **1986**, *264*, 305.
(20) Bonart, R.; Hoffmann, K. *Colloid Polym. Sci.* **1984**, *262*, 1.
(21) Lin, S. B.; Hwang, K. S.; Tsay, S. Y.; Cooper, S. L. *Colloid Polym. Sci.* **1985**, *2*, 128.
(22) Siesler, H. W. *Ber. Bunsen-Ges. Phys. Chem.* **1988**, *92*, 641.
(23) Shinzo, K.; Yuko, I.; Shinzo, Y.; Shibayama, M.; Tetsuo, K.; Shunji, N. *Polym. J.* **1991**, *23*, 991.

(24) Kornfield, J. A.; Spiess, H. W.; Nefzger, H.; Hayen, H.; Eisenbach, C. D. *Macromolecules* **1991**, *29*, 4787.

(25) Reynolds, N.; Spiess, H. W.; Hayen, H.; Nefzger, H.; Eisenbach, C. D. *Macromol. Chem. Phys.* **1994**, *195*, 2855.

(26) Wang, H.; Graff, D. K.; Schoonover, J. R.; Palmer, R. A. *Appl. Spectrosc.* **1999**, *53*, 687.

(27) Chase, B. Private communication.

(28) Desper, C. R.; Schneider, N. S.; Jasinski, J. P.; Lin, J. S. *Macromolecules* **1985**, *18*, 2755.

(29) Shibayama, M.; Toshihito, K.; Tetsuo, K.; Shunji, N.; Takehisa, M. *Polym. J.* **1986**, *18*, 719.

(30) Lee, H. S.; Hsu, S. L. *J. Polym. Sci., Part B: Polym. Phys.* **1994**, *32*, 2085.

(31) Khranovskii, V. A.; Gulko, P. L. *J. Macromol. Sci., Phys.* **1983**, *22*, 497.

(32) Le Grand, D. G.; Erhardt, P. F. *Trans. Soc. Rheol.* **1962**, *6*, 301.

(33) Read, B. E. *Polymer* **1962**, *3*, 143.

(34) Stein, R. S. *J. Polym. Sci.* **1966**, *C15*, 185.

(35) Wilkes, C. E.; Yusek, C. S. *J. Macromol. Sci., Phys.* **1973**, *7*, 157.

(36) Fakirov, S.; Apostolov, A. A.; Boeseke, P.; Zachmann, H. G. *J. Macromol. Sci., Phys.* **1990**, *29*, 379.

(37) Apostolov, A. A.; Fakirov, *J. Macromol. Sci., Phys.* **1992**, *31*, 329.

(38) Fakirov, S.; Fakirov, C.; Fischer, E. W.; Stamm, M.; Apostolov, A. A. *Colloid Polym. Sci.* **1993**, *271*, 811.

(39) Stribeck, N.; Sapoundjieva, D.; Denchev, Z.; Apostolov, A. A.; Zachmann, H. G.; Stamm, M.; Fakirov, S. *Macromolecules* **1997**, *30*, 1329.

(40) Stribeck, N. *J. Polym. Sci., Polym. Phys.* **1999**, *37*, 975.

(41) Li, H.; White, J. L. *Polym. Sci. Eng.* **2000**, *40*, 917.

(42) Blundell, D.; Eeckhaut, G.; Fuller, W.; Mahendrasingam, A.; Martin, C. *Polymer* **2002**, *43*, 5197.

(43) West, J.; Cooper, S. L. *J. Polym. Sci., Polym. Symp.* **1977**, *60*, 127.

(44) Shibayama, M.; Ohki, Y.; Kotani, T.; Nomura, S. *Polym. J.* **1987**, *19*, 1067.

(45) Fakirov, S.; Denchev. Z.; Apostolov, A. A.; Stamm, M.; Fakirov, C. *Colloid Polym. Sci.* **1994**, *272*, 1363.

(46) Lin. S. B.; Hwang, K. S.; Tsay, S. Y.; Cooper, S. L. *Colloid Polym. Sci.* **1985**, *263*, 128.

(47) Wang, C. B.; Cooper, S. L. *Macromolecules* **1983**, *16*, 775.

(48) Moreland, J. C.; Wilkes, G. L.; Turner, R. B. *J. Appl. Polym. Sci.* **1991**, *43*, 801.

(49) Sakurai, S.; Okamoto, Y.; Sakaue, H.; Nakamura, T.; Banda, L.; Nomura, S. *J. Polym. Sci., Part B: Polym. Phys.* **2000**, *38*, 1716.

(50) Chu, B.; Hsiao, B. S. *Chem. Rev.* **2001**, *101*, 1727.

(51) Fraser, R. D. B. *J. Chem. Phys.* **1958**, *28*, 1113.

(52) Siesler, H. W.; Holland-Moritz, K. *Infrared and Raman Spectroscopy of Polymers;* Marcel Dekker: New York, 1980.

(53) Ishihara, H.; Kimura, I.; Yoshihara, N. *J. Macromol. Sci., Phys.* **1983**, *B22*, 713.

(54) Wang, C. B.; Cooper, S. L. *Macromolecules* **1983**, *16*, 775.

(55) McLean, R. S.; Sauer, B. B. *J. Polym. Sci., Polym. Phys. Ed.* **1999**, *37*, 859.

(56) Nakayama, K.; Ino, T.; Matsubara, I. *J. Macromol. Sci., Chem.* **1969**, *5*, 1005.

(57) Coleman, M. M.; Lee, K. H.; Skrovanek, D. J.; Painter, P. C. *Macromolecules* **1986**, *19*, 214.

(58) Blackwell, J.; Nagarajan, M. R.; Hoitink, T. B. *Polymer* **1981**, *22*, 1534.

(59) Born, L.; Hespe, H.; Crone, J.; Wolf, K. H. *Colloid Polym. Sci.* **1982**, *260*, 819.

(60) Tadokoro, H.; Kobayashi, M. In *Polymer Spectroscopy*; Hummel, D. O., Ed.; Verlag Chemie: Weinheim, 1974; p 1.

(61) Miller, J. A.; Lin, S. B.; Hwang, K. K. S.; Wu, K. S.; Gibson, P. E.; Cooper, S. L. *Macromolecules* **1985**, *18*, 32 and references therein.

(62) Sung, C. S. P.; Smith, T. W.; Sung, N. H. *Macromolecules* **1980**, *13*, 117.

(63) Garrett, J. P.; Runt, J.; Lin, J. S. *Macromolecules* **2000**, *33*, 6353.

(64) Miller, J. A.; Cooper, S. L.; Han, C. C.; Pruckmayr, G. *Macromolecules* **1984**, *17*, 1063.

(65) Sauer, B. B.; McLean, R. S.; Brill, D. J.; Londono, J. D. *J. Polym. Sci., Polym. Phys.* **2002**, *40*, 1727.

(66) Sauer, B. B. Unpublished data.

(67) Gerasimov, V. I.; Genin, Ya. V.; Kitaigorodsky, A. I.; Gower, L. A.; Tsvankin, D. Ya. *Kolloid Z. Z. Polym.* **1972**, *250*, 518.

MA0214456